International Journal of Heat and Mass Transfer 159 (2020) 120098

Contents lists available at ScienceDirect

International Journal of Heat and Mass Transfer

journal homepage: www.elsevier.com/locate/hmt

Temporal secondary stability simulation of Rayleigh-Bénard-Poiseuille flow

Md Kamrul Hasan*, Andreas Gross

Mechanical and Aerospace Engineering Department, New Mexico State University, Las Cruces, NM 88003, New Mexico

ARTICLE INFO

Article history:
Received 6 February 2020
Revised 11 June 2020
Accepted 19 June 2020

Keywords:
Rayleigh-Bénard-Poiseuille flows
Secondary instability
Temporal stability simulation

ABSTRACT

The onset of primary and secondary instability has important implications for Rayleigh-Bénard-Poiseuille flows. This paper demonstrates that the primary and secondary instability can be investigated with temporal simulations based on the full and linearized Navier-Stokes equations. Three cases with subcritical Reynolds number and supercritical Rayleigh number are discussed. It is shown that the secondary instability results from a triad interaction of the fundamental steady three-dimensional mode with a two-dimensional and two oblique modes. As the disturbances grow to non-linear amplitudes, the longitudinal rolls exhibit a sinusoidal wavy deformation. The wavelength of the most amplified secondary instability wave is in good agreement with experimental observations. The phase speed of the waves is close to the basic flow bulk velocity as suggested in the literature.

1. Introduction

Rayleigh-Bénard-Poiseuille (RBP) flows occur in nature and have many technical applications. Examples are the flow through the collector of solar chimney power plants [1] and through chemical vapor deposition reactors [2,3]. The buoyancy-driven instability of RBP flow have been investigated in considerable detail. Gage and Reid [4] employed linear stability theory (LST) to investigate the buoyancy- and viscosity-driven instability of plane RBP flow. The two relevant dimensionless numbers are the Reynolds number,

$$Re = \frac{u_{max} h/2}{\nu}, \tag{1}$$

where $u_{\max}$ is the channel maximum velocity, $h/2$ is the channel half-height, and ν is the kinematic viscosity, and the Rayleigh number,

$$Ra = \frac{g h^3 \gamma \Delta T}{\nu \alpha^*}, \tag{2}$$

with gravitational acceleration, g, volumetric thermal expansion coefficient, γ, temperature difference, ΔT, and thermal diffusivity, α^*. According to Gage and Reid [4], buoyancy-driven instability occurs for $Ra > Ra_c = 1708$ and viscosity-driven instability occurs for $Re > Re_c = 5400$. Orszag [5] later found a more accurate value for the critical Reynolds number for the onset of the viscosity-driven instability of 5772.22. A linear stability analysis by Fujimura and Kelly [6] revealed that for Reynolds numbers in the range $0.01 \leq Re \leq 100$, the critical Rayleigh number for two-dimensional (2-D) unstable waves was increasing with Reynolds number. This finding is essentially consistent with the zero degree wave angle neutral curve by Gage and Reid [4]. According to Luijkx et al. [7], below a minimum finite aspect ratio, transverse rolls that are aligned perpendicular to the flow direction can occur for $Ra > Ra_c$ and $Re < Re_c$. Nevertheless, in general for $Re < Re_c$ buoyancy-driven instability leads to the emergence of counter-rotating longitudinal vortices which are referred to as longitudinal rolls. The appearance of such longitudinal rolls in plane RBP flow has also been confirmed by many experimental investigations [8,9].

When the disturbance amplitudes associated with the primary instability get sufficiently high and non-linear interactions become important, secondary instability can occur. Clever and Busse [10] were the first to carry out a secondary linear stability analysis for longitudinal rolls in a RBP flow with infinite spanwise extent and found two distinct modes of secondary instability. The first mode is known as wavy instability and occurs above a critical Rayleigh number. The streamwise wavenumber, $\alpha = 2\pi/\lambda_x$, with streamwise wavelength, λ_x, of this mode increases with Rayleigh number. As the Rayleigh number is raised above the critical Rayleigh number, the wavy instability initially occurs for very small α. The second mode is referred to as the oscillatory instability and occurs for low Reynolds numbers and high Rayleigh numbers. Kato and Fujimura [11] performed a LST analysis of a finite span square channel RBP flow and found a higher critical Rayleigh number for the onset of the wavy instability than for an infinite

* Corresponding author.
E-mail address: kamrul04@nmsu.edu (M.K. Hasan).

https://doi.org/10.1016/j.ijheatmasstransfer.2020.120098
0017-9310/

span RBP flow. An experimental investigation of the wavy instability for a case with fully developed longitudinal rolls was carried out by Pabiou et al. [12]. Because of the convective nature of the secondary instability, they employed localized upstream harmonic forcing to raise the initial amplitude of the secondary instability waves. The phase speed of the most amplified secondary instability waves was found to be very close to the bulk velocity and the wavelength was shown to increase with decreasing Rayleigh number. Xin et al. [13] carried out a numerical investigation of the instability of RBP flow for a channel with an aspect ratio (span to height) of 10. The primary instability led to either nine, 10 or 11 longitudinal rolls. All three configurations were subject to the three-dimensional (3-D) wavy instability and a linear relationship between the angular frequency and streamwise wave number was established which confirmed the earlier finding that the wave speed approximately matches the bulk velocity. Nicolas et al. [14] employed LST and direct numerical simulations (DNS) for investigating the finite-span effect on the instability of RBP flows. They found that the critical Rayleigh number for the onset of the wavy instability for a finite aspect ratio of 10 is approximately 1.5 - 1.8 times higher than for an infinite aspect ratio channel.

This paper reports on temporal secondary instability investigations of plane RBP flows with infinite spanwise extent and fully established longitudinal rolls. The stability investigations were carried out with high-order-accurate codes that solve the full and linearized Navier-Stokes equations. The codes employ a unique combination of a spectral discretization in the homogeneous (streamwise and spanwise) directions, and a high-order discretization in the wall-normal direction. Details about the numerical methods and validation cases can be found in a companion paper [15]. The infinite span assumption, which is implicitly invoked through the use of Fourier modes, allows for a direct comparison with linear stability theory. The primary interest of the present paper is on the wavy secondary instability which leads to the breakdown of the longitudinal vortices resulting from the primary instability. Results are shown for three cases with subcritical Reynolds number and supercritical Rayleigh number. The paper concludes with a brief summary and discussion of the results.

2. Methodology

2.1. Computational method

The present numerical Rayleigh-Bénard-Poiseuille (RBP) stability investigations were carried out with high-order-accurate codes that solve the full and linearized compressible Navier-Stokes equations. The two approaches are here referred to as direct numerical simulation (DNS) and linearized Navier-Stokes simulation (LNS). For both, a forcing term was added to the right-hand-side of the streamwise momentum equation to compensate for the streamwise pressure drop and the Boussinesq approximation was invoked for the buoyancy acceleration in the vertical direction. The top and bottom wall temperature were considered as isothermal. The governing equations were made dimensionless with a reference velocity, u_{ref}, reference length, L_{ref}, reference temperature, $T_{ref} = 300K$, and reference density, ρ_{ref}. Pressure was non-dimensionalized with $\rho_{ref} u_{\max}^2$. Unless stated otherwise, the maximum velocity, $u_{\max}$, and channel half-height, $h/2$, were taken as reference velocity and reference length. The reference Mach number was $M = 0.1$. Fourier transforms were employed in the two homogeneous directions (streamwise and spanwise). The convective and viscous terms in the wall-normal direction were evaluated with fifth- and fourth-order-accurate compact finite differences for non-equidistant grids, respectively. A fourth-order-accurate-Runge-Kutta scheme was employed for time integration. Details regarding the governing equations, the discretization and the boundary conditions can be found in Hasan and Gross [15].

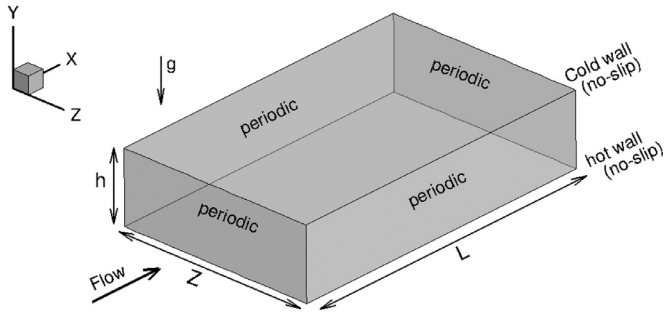

Fig. 1. Three-dimensional computational domain.

2.2. Computational grid

Grid points were clustered near the top and bottom wall using an analytical wall-normal grid point distribution,

$$y_j = \left[\frac{\tan^{-1}(jc^* - f_1)}{f_2} + 1 \right] \frac{h}{2}. \tag{3}$$

Here j is the wall-normal grid line index and J is the total number of grid points, $h = 2$ is the channel height, $c^* = 0.05$ is a user-specified constant, $f_1 = Jc^*/2$, and $f_2 = \tan^{-1}(f_1)$. The streamwise and spanwise domain extent of the computational grid are denoted by L and Z, respectively. A sketch of the 3-D computational domain indicating the coordinate system, geometric dimensions, boundary conditions, as well as the direction of the flow and the gravitional acceleration is shown in Fig. 1.

2.3. Basic flow

The basic flow for the simulations was obtained by solving the one-dimensional (1-D) Navier-Stokes equations,

$$\frac{\partial p}{\partial x} = \mu \frac{\partial^2 u}{\partial y^2}, \tag{4}$$

$$\frac{\partial p}{\partial y} = (1 - \rho) g, \tag{5}$$

$$k \frac{\partial^2 T}{\partial y^2} + \mu \left(\frac{\partial u}{\partial y} \right)^2 = 0, \tag{6}$$

with a second-order-accurate shooting method. Very small (linear) random disturbances slightly above machine roundoff were added to the basic flow to raise the initial disturbance amplitudes for the stability analyses.

2.4. Numerical linear stability analysis

According to temporal Linear Stability Theory (LST), a wave ansatz of the form

$$u_i'(x, y, z, t) = \sum \hat{u}_i(y) e^{i(\alpha x + \beta z - \omega t)}, \tag{7}$$

can be made for the disturbances where α, β and $\omega = \omega_r + i\omega_i$ are the streamwise and spanwise wavenumber as well as the angular frequency. Here, $\hat{u}_i(y)$ are the mode amplitude distributions. The streamwise, λ_x, and spanwise, λ_z, wavelengths can be obtained from the streamwise and spanwise wavenumbers, $\lambda_x = 2\pi/\alpha$ and $\lambda_z = 2\pi/\beta$. The wavelengths λ_x and λ_z are related to the streamwise, L, and spanwise domain extent, Z, via $\lambda_x = L/l$ and $\lambda_z = Z/m$, where l and m are the streamwise and spanwise Fourier mode

Table 1
Parameters for stability simulations.

	Re	*Ra*
Validation case (Pabiou et al. [12])	87	6300
Case 1	130.5	8000
Case 2	130.5	5000

number. The period, T_p, is related to the real part of the angular frequency via $T_p = 2\pi/\omega_r$. Throughout the paper Fourier modes are referred to as (l, m). The wavelength and wavenumber in the wave propagation direction are $\lambda = 2\pi/k_\lambda$ and $k_\lambda = \sqrt{\alpha^2 + \beta^2}$ and the wave angle is $\theta = \tan^{-1}(\beta/\alpha) = \tan^{-1}(\lambda_x/\lambda_z)$. For oblique waves, the amplitude, A, and phase, ψ, of the left and right-traveling waves (in negative and positive z-direction) is denoted by a "-" and "+" superscript. The disturbance amplitude, A, was computed as the square root of the disturbance kinetic energy, $A = \sqrt{E'}$, which was averaged over the channel height,

$$E' = \frac{1}{2h}\int_0^h \left[\hat{u}^2(y) + \hat{v}^2(y) + \hat{w}^2(y)\right] \mathrm{d}y. \tag{8}$$

This criterion was demonstrated to accurately characterize the growth of disturbance waves [16,17]. The temporal growth rates were obtained from,

$$\omega_i = \frac{d[\ln(\frac{A}{A_0})]}{dt}, \tag{9}$$

where A_0 is the disturbance amplitude at $t = 0$ and the phase speed in the x-direction was computed as

$$c_x = -\frac{\frac{\partial\psi}{\partial t}}{\frac{\partial\psi}{\partial x}} = \frac{\omega_r}{\alpha}, \tag{10}$$

where $\psi = \alpha x + \beta z - \omega_r t$. The phase speed in the wave propagation direction is $c = \omega_r/k_\lambda$. The phase, frequency and phase speed were calculated from the streamwise, wall-normal and spanwise velocity components in the center of the channel.

3. Results

Three cases with buoyancy-driven instability were considered (Table 1). According to Orszag [5] and Gage and Reid [4], the chosen Reynolds numbers are subcritical ($Re < Re_c = 5772.22$) and the Rayleigh numbers are supercritical ($Ra > Ra_c = 1708$). Based on a grid convergence study [15], the number of grid points in the wall-normal direction was set to $J = 72$.

3.1. Validation case

Pabiou et al. [12] carried out an experimental investigation of the secondary instability of RBP flows for $Re_{b1} \geq 100$ and $Ra \geq 6300$, where Re_{b1} is based on the bulk velocity and channel height. One of the cases ($Re_{b1} = 174$ based on channel height or $Re_{b2} = 87$ based on channel half-height and $Ra = 6300$) from the paper by Pabiou et al. [12] was computed for additional validation of the DNS code. For this case and different from the other cases, all quantities were made dimensionless with the bulk velocity and channel half-height. In order to reproduce the experimental case, an appropriate basic flow had to be generated. First, several DNS were performed to find the spanwise wavelength, λ_z, for which the primary mode (longitudinal rolls) was most strongly amplified. According to Fig. 2 a, this occurs for $\lambda_z = 3.22$ ($\beta = 1.9512$). Next, a DNS with eight spanwise modes and $Z = 3.22$ was carried out for $Re_{b2} = 87$ and $Ra = 6300$. The primary mode (0, 1) exhibits linear (i.e. exponential) growth (Fig. 2 b). Non-linear interactions for $t_0 > 140$ lead to the growth of higher harmonics (0, 2), etc. It should be mentioned that non-linear interactions such as $(0,1) + (0,1) = (0,2)$ are always present in the DNS. The amplitude of the resulting modes scales with the product of the amplitudes of the generating modes, e.g. $A(0,2) = A(0,1) \times A(0,1)$. Thus, for the present case, the amplitude of mode (0, 2) grows above 10^{-12} when the amplitude of mode (0, 1) surpasses 10^{-6}. Around $t_0 = 350$ all mode amplitudes saturate. An instantaneous flow field at $t_0 = 400$ obtained from this precursor simulation was taken as 3-D basic flow for a secondary instability investigation.

Next, a wavelength study was conducted to find the most amplified secondary instability mode. According to Fig. 3 a, the most unstable 2-D mode has a streamwise wavelength of $\lambda_x = 9$ or $\lambda_x = 4.5$ based on channel height which is in close agreement with the experimental measurements by Pabiou et al. [12]. The corresponding streamwise wavenumber is $\alpha = 0.698$ (1.40 based on channel height) and the temporal growth rate is $\omega_i = 0.0407$. In Fig. 3 b the phase speed in the x-direction is plotted versus the ratio of the streamwise wavelength and channel height. The most amplified secondary instability mode has a phase speed of $c_x = 0.94$. Pabiou et al. [12] measured a phase speed of $1.1u_b \pm 7\%$. A linear stability analysis by Clever and Busse [10] suggests that the phase speed is within a few percent of the bulk velocity. The present result is thus in reasonable agreement with the published literature.

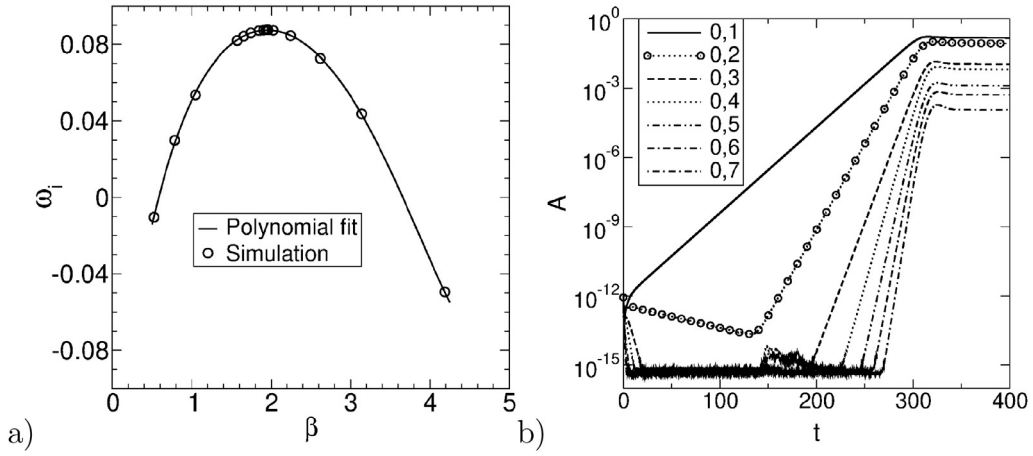

Fig. 2. a) Wavelength study: temporal growth rate versus spanwise wavenumber and b) Amplitude vs. time for primary wave and higher harmonics for $Re_{b2} = 87$ and $Ra = 6300$. The saturated flow at $t_0 = 400$ is used as baseflow for the secondary instability investigation.

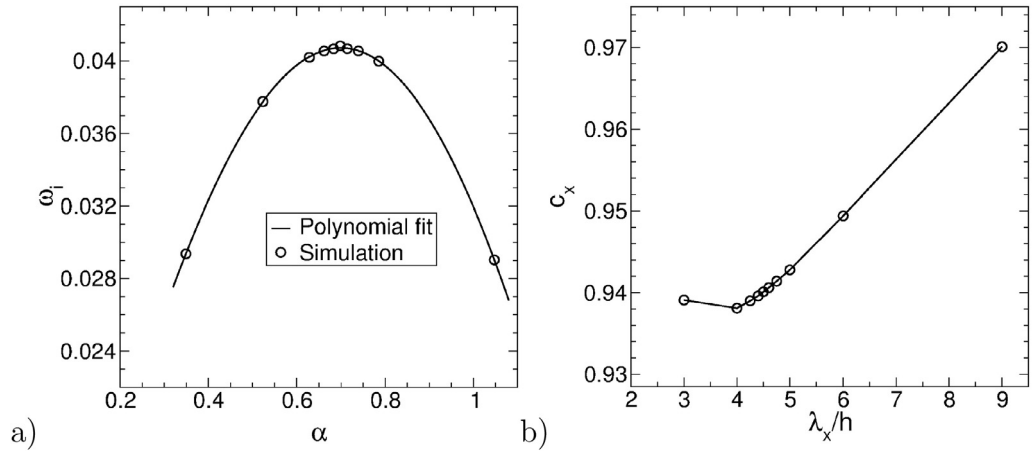

Fig. 3. Dependence of a) growth rate and b) phase speed (data points are connected by straight lines) of secondary unstable 2-D mode on streamwise wavenumber and wavelength for $Re_{b2} = 87$ and $Ra = 6300$.

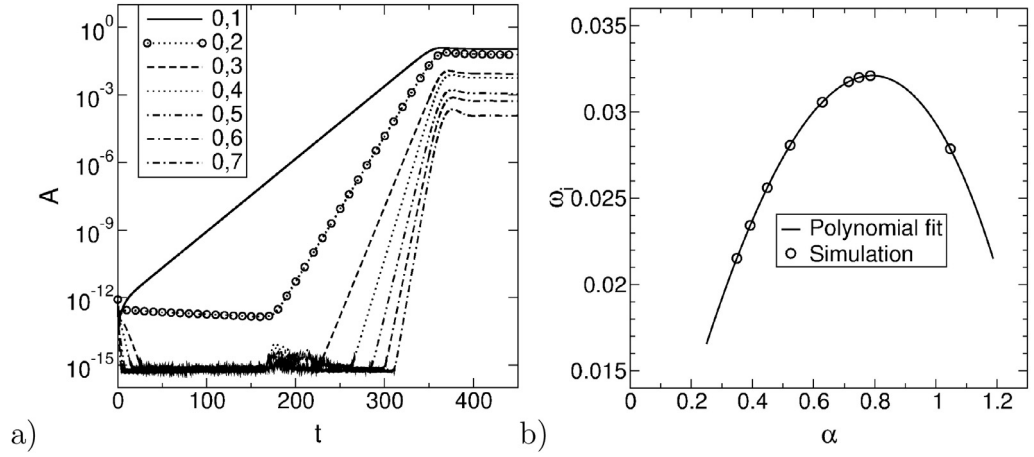

Fig. 4. a) Primary mode amplitude versus time and b) growth rate of unstable 2-D secondary mode versus streamwise wavenumber for case 1.

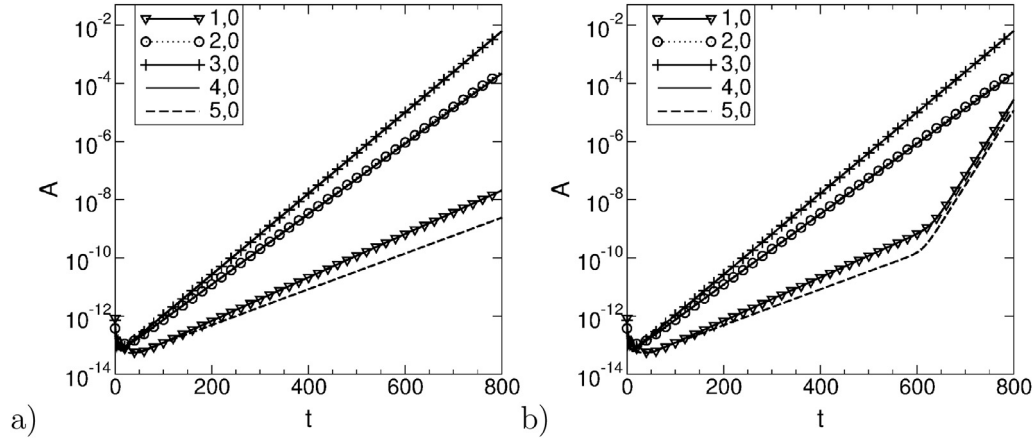

Fig. 5. Amplitude of secondary unstable 2-D mode versus time for case 1: a) LNS and b) DNS.

3.2. Case 1: Increased Rayleigh number

The Reynolds and Rayleigh number were set to $Re = 130.5$ and $Ra = 8000$. According to the stability boundary by Clever and Busse [10], this case should exhibit secondary instability. The bulk Reynolds number based on channel half-height (Re_{b2}) is approximately 87. As for the validation case, precursor simulations were carried out to determine the spanwise wavelength ($\lambda_z = 3.1$) for which the 3-D primary mode experienced the strongest amplification. Next, a DNS with spanwise domain extent of $Z = 3.1$ and eight modes in the spanwise direction was performed. The temporal development of the spanwise mode amplitudes is shown in Fig. 4 a. Once the primary mode (0, 1) with $\lambda_z = 3.1$ reaches a sufficiently high amplitude, the higher harmonics (0, 2), (0, 3), etc.

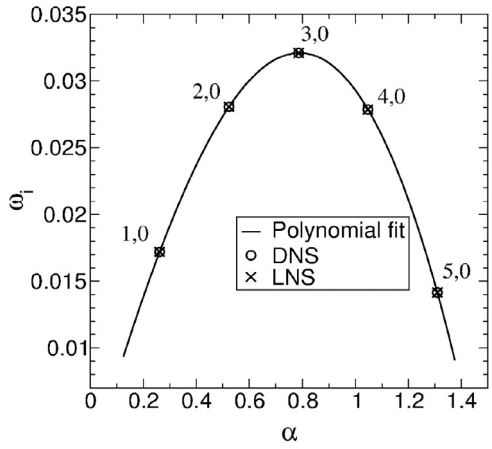

Fig. 6. Growth rates of 2-D modes versus streamwise wavenumber (linear regime) for case 1.

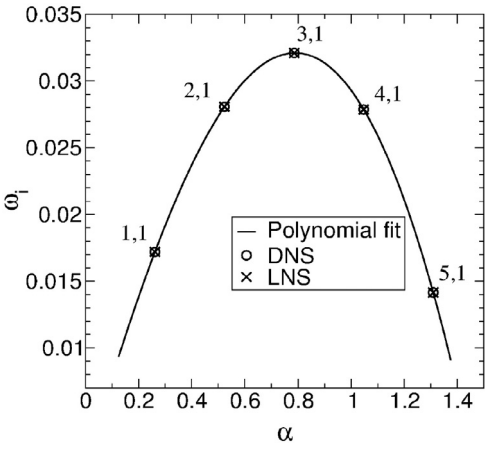

Fig. 8. Growth rates of 3-D right-traveling modes versus streamwise wavenumber (linear regime) for case 1.

begin to grow. At $t_0 = 450$ the mode amplitudes are saturated and a steady 3-D flow with fully developed longitudinal vortices is obtained which is then used as basic flow for the secondary instability analysis. A streamwise wavelength study was carried out to determine the streamwise wavelength for which the secondary instability waves experience the strongest amplification. Fig. 4b reveals that the largest secondary growth ($\omega_i = 0.0321$) is obtained for a streamwise wavelength of $\lambda_x = 8$ ($\lambda_x = 4$ based on channel height) and a streamwise wavenumber of $\alpha = 0.785$ (1.57 based on channel height). Because time was made dimensionless with the ratio of reference length and reference velocity, the temporal growth rate based on the bulk velocity can be computed from the temporal growth rate based on the maximum velocity via $(\omega_i)_{bulk} = (u_{\max}/u_b)(\omega_i)_{\max}$. For the present case $(\omega_i)_{bulk} = 0.04815$ is obtained which is greater than the secondary growth rate for $Re_{b2} = 87$ and $Ra = 6300$ (validation case for secondary instability). Based on the comparison with the validation case, it is also found that as the Rayleigh number increases, the streamwise wavelength of the most amplified secondary instability wave is reduced. The higher temporal growth rate and lower streamwise wavelength are in agreement with Clever and Busse [10] and Pabiou et al. [12].

After the most unstable streamwise wavelength was determined, additional LNS and DNS were carried out for $Re = 130.5$ and $Ra = 8000$. For these simulations, the streamwise and spanwise domain extent were set to $L = 3 \times \lambda_x = 24$ and $Z = \lambda_z = 3.1$ and a total of 16 and eight modes were employed in the streamwise and spanwise direction. In Fig. 5, the 2-D mode amplitude distributions are plotted over time. Mode (3, 0), which has a streamwise wavelength of $\lambda_x = 8$, displays the strongest linear growth. Other modes also exhibit linear growth but the growth rates are lower than for mode (3, 0). The always present non-linear interaction of mode (3, 0) and $\pm$ (2, 0) in the DNS leads to the growth of modes (5, 0) and (1, 0) for $t > 600$. This effect only becomes visible for $t > 600$ when the nonlinearly generated amplitudes, which scale approximately with $A(3, 0) \times A(2, 0)$, exceed the linear growth amplitudes of modes (5, 0) and (1, 0). The growth rates of the 2-D modes obtained from the LNS and DNS are in excellent agreement for $t < 600$ (see Fig. 6). Fig. 7 shows the time evolution of the disturbance amplitudes of the right-traveling oblique waves. In Fig. 8, the temporal growth rate is plotted versus the streamwise wavenumber. For $t < 600$ the growth rates obtained from the LNS and DNS are identical which provides proof that the secondary growth is in fact linear. Mode (3, 1) which has a streamwise wavelength of $\lambda_x = 8$ and a spanwise wavelength of $\lambda_z = 3.1$ grows the fastest. The amplitudes and growth rates of the left-traveling oblique waves are virtually identical to those of the right-traveling oblique waves (Figs. 9 & 10) since the basic flow is symmetric. It can also be noted that the growth rates of modes (3, 0), (3, 1), and $(3, -1)$ are identical ($\omega_i = 0.0321$). To help understand this phenomenon, in Fig. 11 the growth rates, frequencies, and phase speeds of modes (3, 0), (3, 1) and $(3, -1)$ are plotted versus time. As in resonance triads for fundamental boundary layer breakdown [18], the primary spanwise mode (0, 1) and the secondary modes

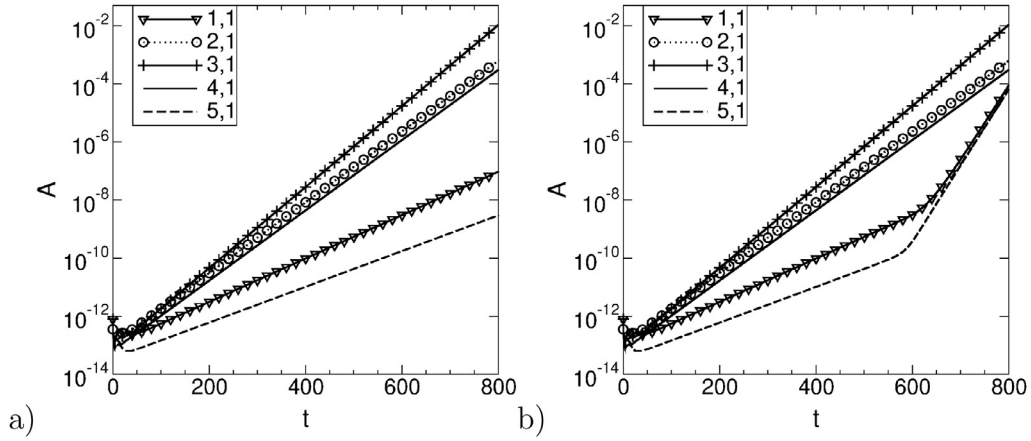

Fig. 7. Amplitude of secondary unstable 3-D right-traveling mode versus time for case 1: a) LNS and b) DNS.

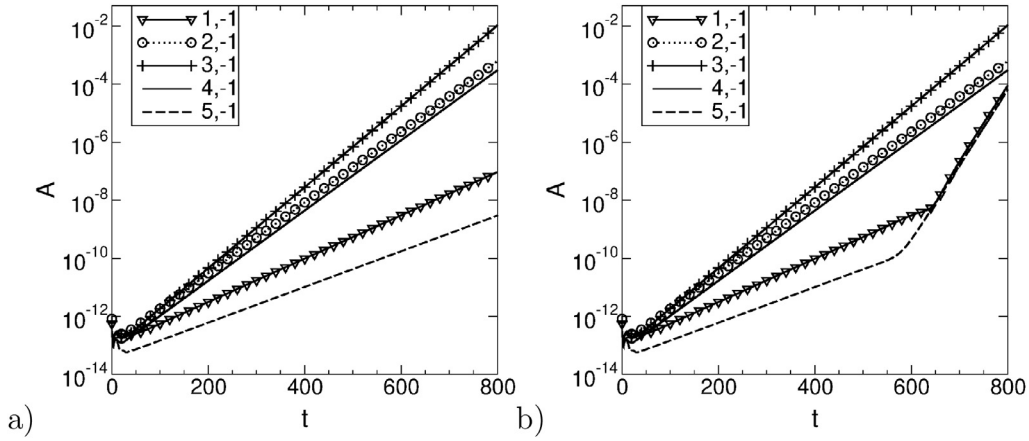

Fig. 9. Amplitude of secondary unstable 3-D left-traveling mode versus time for case 1: a) LNS and b) DNS.

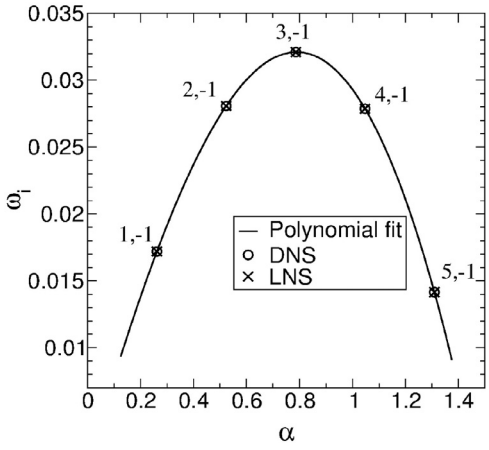

Fig. 10. Growth rates of 3-D left-traveling modes versus streamwise wavenumber (linear regime) for case 1.

(3, 0) & (3, ± 1) are linked. The secondary modes share the same growth rate, frequency and phase speed. The phases of the two-dimensional mode and the two oblique modes are aligned in such a fashion that the secondary modes extract energy from the primary mode [18]. Modes (1, 0) & (1, ± 1) and (2, 0) & (2, ± 1) also exhibit triad interactions (not shown).

Fig. 12 displays isocontours of the u', v', and w' disturbance amplitudes for the three streamwise wavelengths $\lambda_x = 24$, 12 and 8 that correspond to modes (1, 0), (2, 0), and (3, 0). Also shown are isocontours of the 3-D component of the basic flow (i.e. all steady spanwise modes). The placement of the streamwise secondary mode disturbance maxima in Fig. 12 relative to the isocontours for the basic flow illustrates which part of the basic flow contributes to the secondary growth. The u' disturbance amplitude for $\lambda_x = 24$ exhibits four maxima at $z \approx 0.052$, 1.03, 1.65, and 2.6 near $y \approx 0.7$ and 1.3 as seen in Fig. 12 a. For $\lambda_x = 12$ and 8 the maxima at $z \approx 1.03$ and 1.65 are shifted upward while the other two maxima at $z \approx 0.052$ and 2.6 are shifted downward (Fig. 12 b and Fig. 12 c). The v' amplitude distribution has two maxima, however the shift of the maxima towards the shorter wavelengths is minimal (Figs. 12 d-12 f). Figs. 12 g-12 i display four maxima of the w' disturbance amplitude distributions. For the shorter streamwise wavelength, the maxima are shifted farther away from the center of the channel and sideways.

Fig. 13 shows isosurfaces of the Q-criterion [19] flooded by the streamwise vorticity for $t = 800$. As a result of the secondary instability, the straight longitudinal rolls (basic flow) become wavy as also observed in the experiment by Pabiou et al. [12]. The u', v', w', and T' disturbance amplitude distributions for the primary and secondary modes at $t = 500$ are plotted in Fig. 14. The mode shapes obtained from the LNS and DNS are in close agreement which again is evidence that the secondary instability results from a linear resonance. The shape of the 2-D secondary mode (3, 0) is noticeably different from that of the primary mode (0, 1). For example, the v' amplitude distribution for mode (3, 0) features two peaks while the primary mode has only one peak at $y \approx 1$. On the

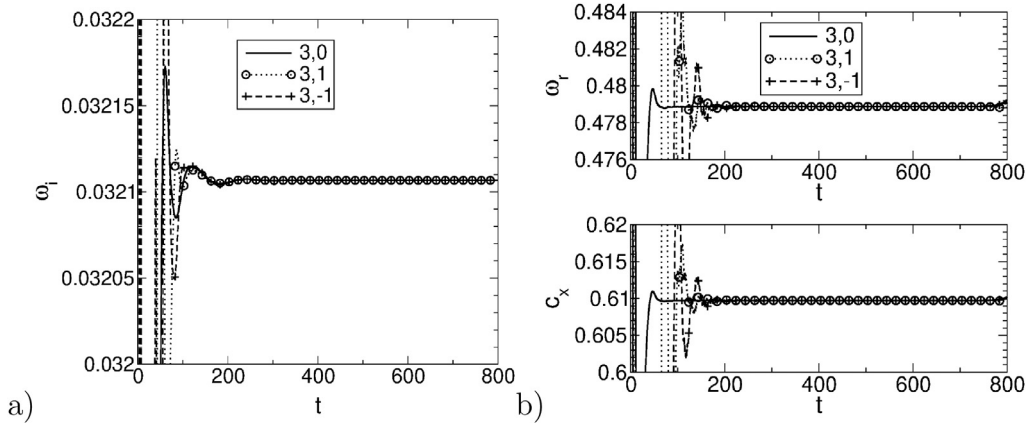

Fig. 11. a) Growth rate and b) frequency & phase speed distributions versus time for modes (3, 0), (3, 1) & (3, −1) (case 1).

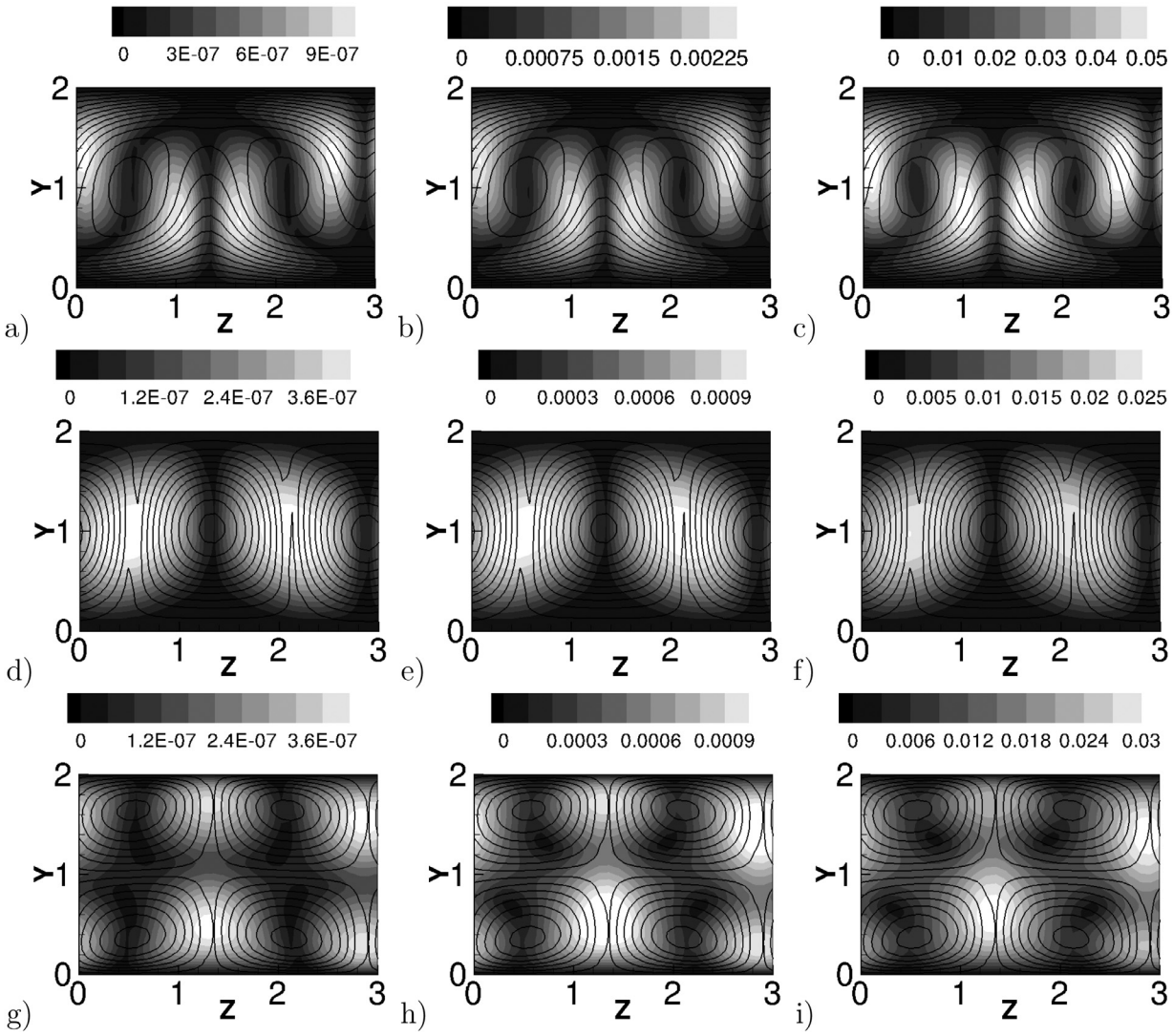

Fig. 12. Isocontours of u' (a - c), v' (d - f), and w' (g - i) distrubance amplitude (grey scales) plotted over isocontours of 3-D component of basic flow (solid lines) for streamwise wavelength of $\lambda_x = 24$ (a, d, g), 12 (b, e, h) and 8 (c, f, i), respectively. The range and spacing of the isocontours for the basic flow is 0 to 0.78 with $\Delta = 0.06$ for u', -0.14 to 0.14 with $\Delta = 0.0147$ for v', and -0.12 to 0.12 with $\Delta = 0.016$ for w'.

other hand, the differences between the primary mode (0, 1) and the oblique secondary modes (3, $\pm$ 1) are more subtle except for the T' amplitude distribution which has two peaks for the primary mode but only one peak for the oblique modes.

In their experiment, Pabiou et al. [12] investigated the secondary instability of a flow with fully developed longitudinal rolls. This rises the question how well developed the longitudinal rolls need to be for the secondary wavy instability to occur. To answer this question, the basic flow was extracted at different time instances ($t_0 = 300$, $t_0 = 350$ and $t_0 = 450$) from the precursor simulation (Fig. 4 a). For each basic flow, a secondary instability DNS was performed using the same parameters as before ($L = 3 \times \lambda_x = 24$, $Z = \lambda_z = 3.1$, 16 modes in x and 8 modes in z). The mode amplitudes of the 2-D and oblique modes are shown in Figs. 15 a-15 c. It can be seen that the growth rates of modes (1, 0) and (1, $\pm$ 1) are substantially increased for $t_0 = 300$ and $t_0 = 350$ compared to $t_0 = 450$. Figs. 15 d and 15 e provide a clearer picture: The growth rates of mode (1, 0), (1, $\pm$ 1), (2, 0) and (2, $\pm$ 1) are decreasing while the growth rates of modes (3, 0) and (3, $\pm$ 1) are increasing when the amplitude of the primary wave (0, 1) is increased (Fig. 15 d). The phase speeds are provided in Fig. 15 e. Interestingly, as the basic flow 3-D mode amplitude is increased beyond 0.09, the phase speed of the waves suddenly decreases sharply. This reduction in phase speed is most pronounced for (3, 0) and (3, $\pm$ 1). Possible phase-locking of (2, 0) & (2, $\pm$ 1) with (3, 0) & (3, $\pm$ 1) may lead to resonance and energy transfer from the former to the latter.

A similar investigation was also carried out for a basic flow comprised solely of the one-dimensional channel flow and the primary mode (0, 1). The same primary mode amplitudes as for the preceding analysis were considered. Figs. 16 a-16 c show the time evolution of the amplitudes of the 2-D and oblique modes for a basic flow mode (0, 1) amplitude of 0.0024, 0.085 and 0.1098, which correspond to $t_0 = 300$, $t_0 = 350$ and $t_0 = 450$ in Fig. 4 a. Fig. 16 d shows that the 2-D and oblique modes are growing as the result of a triad interaction as for the earlier case (Fig. 15 d). The growth rates of all secondary modes such as (1, 0) and (1, $\pm$ 1) increase as the amplitude of the primary wave is increased (Fig. 16 d). Different from the previous analysis for a basic flow that includes all of the higher steady spanwise modes, modes (1, 0) and (1, $\pm$ 1) remain the most amplified regardless of the basic flow primary mode (0, 1) amplitude. Also different from the previous case, no sudden dramatic reduction of the phase speeds is visible for $A = 0.1098$ (Fig. 16 e). This analysis suggest that a fully developed basic flow is required for the secondary instability to occur.

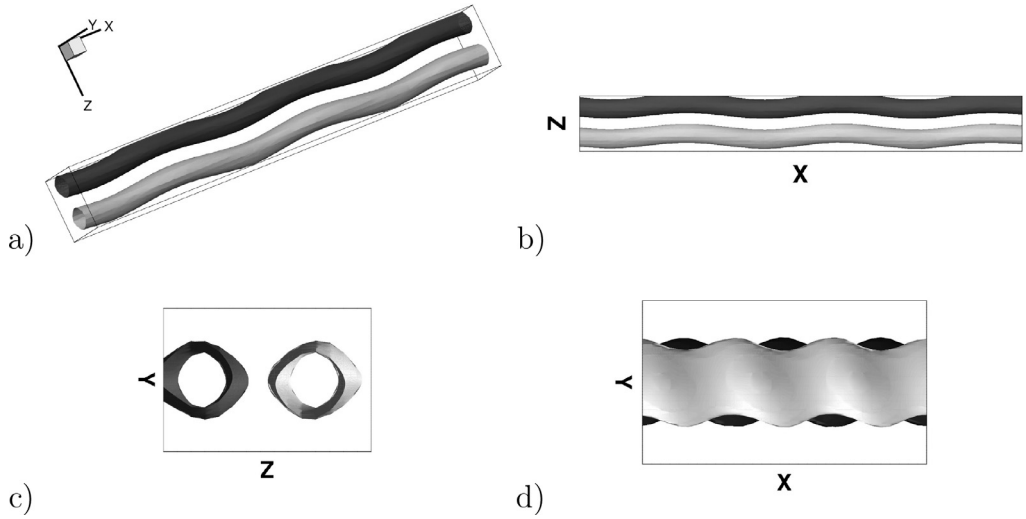

Fig. 13. Isosurfaces of $Q = 0.025$ at $t = 800$ flooded by streamwise vorticity ($\omega_x = \pm 0.4$) for case 1: a) 3-D view, b) top view ($x - z$ plane), c) front view ($y - z$ plane) and d) side view ($x - y$ plane) where x to y ratio is 0.15.

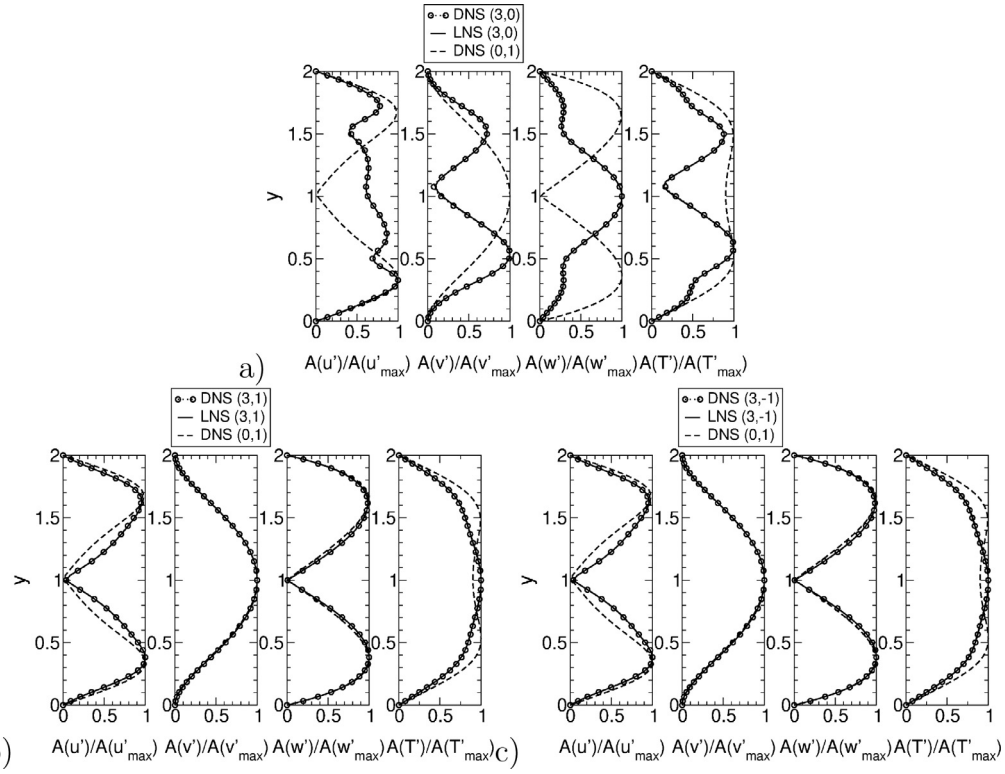

Fig. 14. Distributions of u', v', w', and T' for a) 2-D mode (3, 0), b) right traveling mode (3, 1) and c) left traveling mode $(3, -1)$ at $t = 500$ for case 1. The primary mode (0, 1) is also provided as a reference.

Altough the primary instabiliy for 3-D crossflow and Görtler instability of boundary layer flows is different from the primary instability for plane RBP flow, it leads to steady streamwise vortices. The common feature is that all of them require non-linear saturation of the streamwise vortices for secondary instability to occur [20–23]. However, different from RBP flow, the streamwise vortices resulting from crossflow instability are co-rotating. The crossflow secondary instability leads to the formation of finger vortices [20,21] whereas for RBP flow, the primary longitudinal rolls become wavy in the streamwise direction (sinuous mode). The vortices resulting from Görtler instability are counter-rotating. When Görtler vortices begin to saturate, secondary instability can lead to the growth of varicose and sinuous modes [22–24]. The sinuous mode is indeed analogous to the wavy mode for RBP flow.

Finally, a few words are in place regarding the computational efficiency of the present approach. The present case with 72 wall-normal grid points, eight spanwise Fourier modes and 16 streamwise Fourier modes, was computed on a single core of an Intel Core i7-9700 processor. The computational time required for the

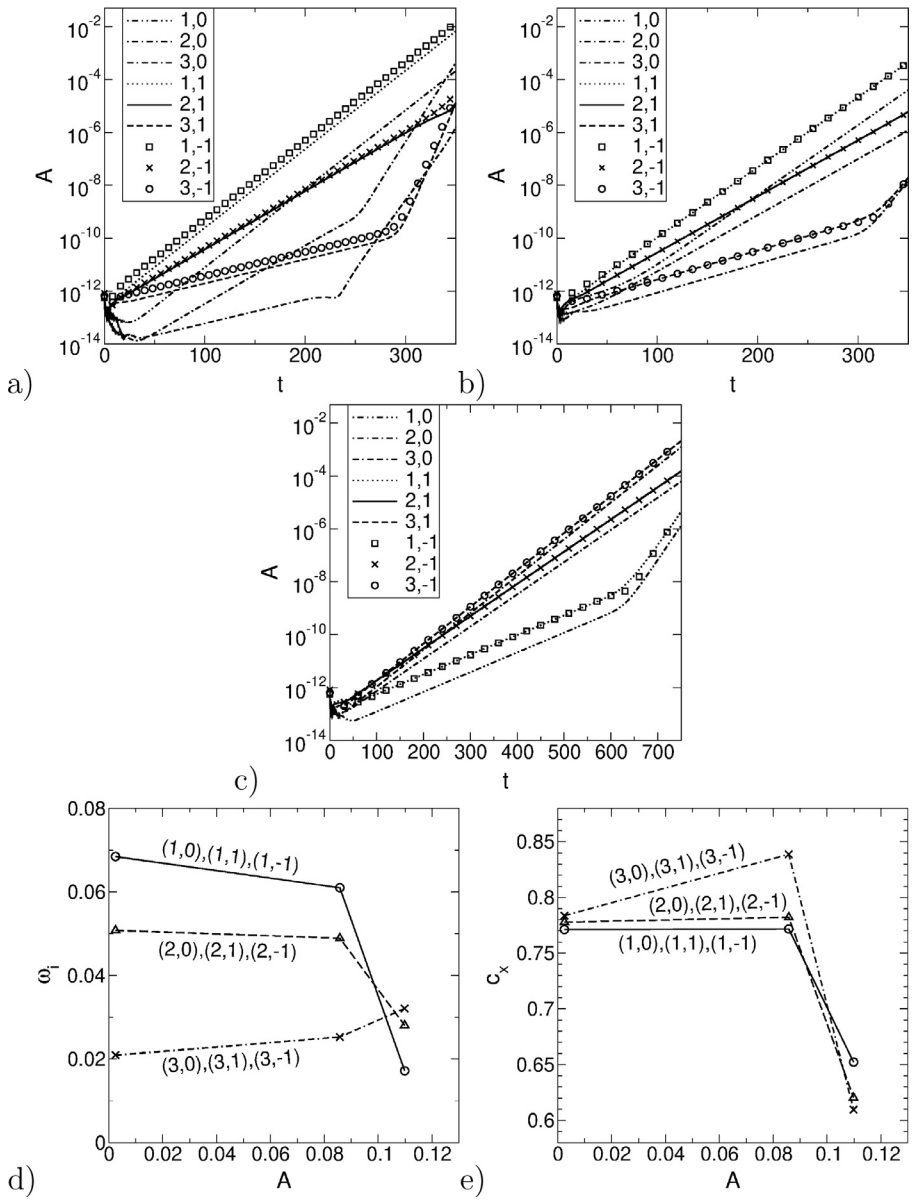

Fig. 15. Mode amplitudes versus time obtained from secondary instability simulations. The basic flow was obtained from the precursor simulation at: a) $t_0 = 300$, b) $t_0 = 350$ & c) $t_0 = 450$. d) Growth rates and e) phase speed of 2-D and 3-D modes versus primary wave amplitude from Fig. 4 a.

growth rates and mode shapes to become fully established is approximately 690 minutes. The corresponding computational time for a single streamwise Fourier mode is thus 690/16 ≈ 43 minutes. The secondary stability analysis can also be formulated as a biglobal problem. As a reference for the required computer time for such an investigation, a biglobal analysis for a rectangular duct flow at $Re = 100$ by Rodríguez and Theofilis [25] shall be considered. Solving for a single mode for a case with 40 × 40 Chebyshev-Gauss-Lobatto points took about 2.5 minutes on four Intel Xeon cores or about 10 minutes on a single core. A more recent publication by Gennaro et al. [26] demonstrates the progress made with regard to the computational efficiency of biglobal stability analysis codes. The solution of a problem with 50 × 50 grid points on a personal computer required only 12.4 seconds.

3.3. Case 2: Reduced Rayleigh number

A similar secondary stability analysis was carried out for a lower Rayleigh number of $Ra = 5000$. The Reynolds number ($Re = 130.5$) and other parameters were kept the same as for case 1. Also, an identical procedure was followed for the analysis. A wavelength study revealed that the primary mode was most unstable for $\lambda_z = 3.4$. A DNS with eight spanwise Fourier modes was performed to obtain a basic flow for the secondary instability investigation. In Fig. 17 a the spanwise mode amplitudes are plotted versus time. The flow field with saturated spanwise modes at $t_0 = 800$ was chosen as basic flow for a secondary instability analysis. Several DNS were carried out with varying streamwise domain extent using two streamwise and eight spanwise Fourier modes. The temporal growth rate of the dominant 2-D mode is shown in Fig. 17 b. For a wavelength of $\lambda_x = 11$ ($\lambda_x = 5.5$ based on channel height) and a corresponding wavenumber of $\alpha = 0.571$ ($\alpha = 1.14$ based on channel height) the 2-D mode is most amplified. The temporal growth rate is $\omega_i = 0.0203$. Compared to case 1 ($Re = 130.5$ and $Ra = 8000$), the streamwise wavelength is increased and the growth rate is reduced. This trend is in agreement with Clever and Busse [10] and Pabiou et al. [12].

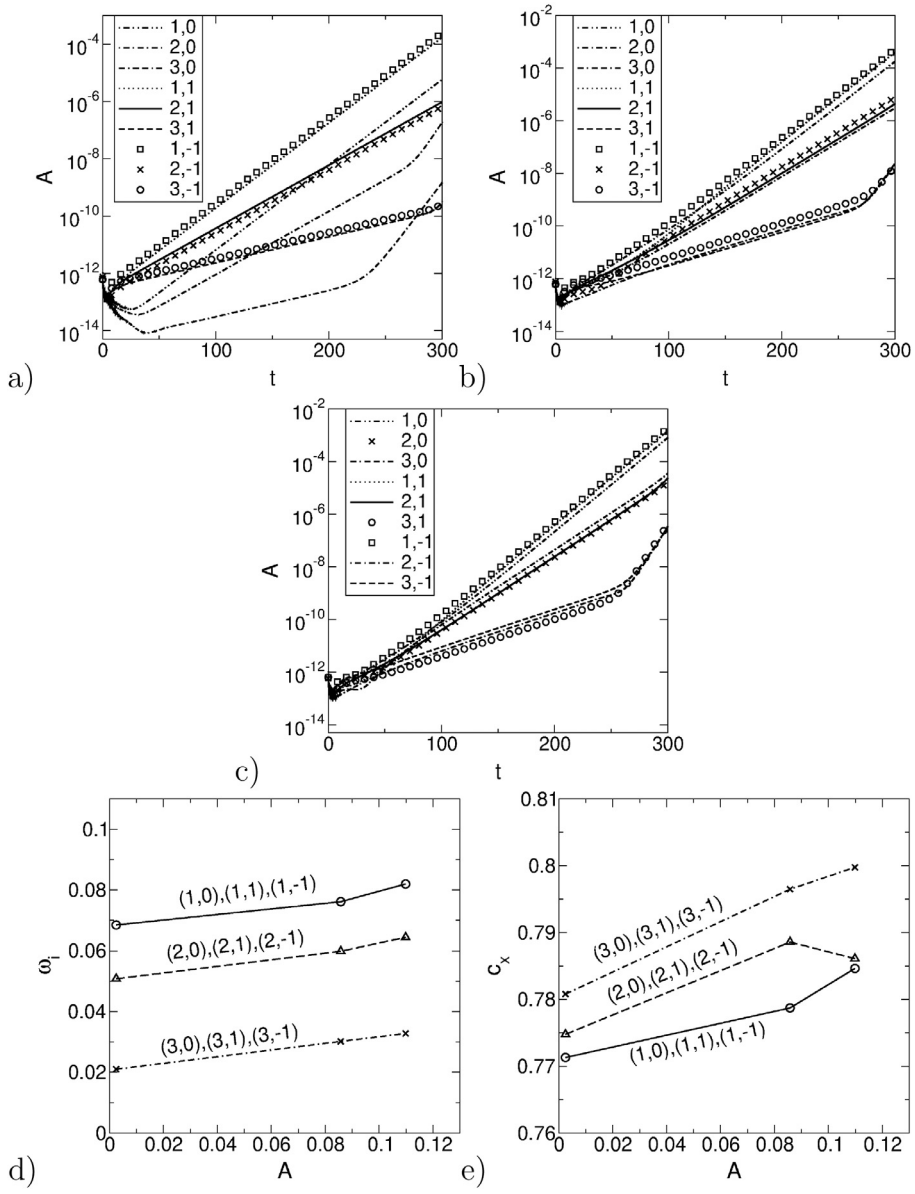

Fig. 16. Mode amplitudes versus time obtained from secondary instability simulations for basic flow comprised of 1-D profile and (0, 1) mode with a) A= 0.0024, b) A= 0.085, and c) A= 0.1098 (corresponding to $t_0 = 300$, $t_0 = 350$ and $t_0 = 450$ in Fig. 4 a). d) Growth rates and e) phase speed of 2-D and 3-D modes versus primary wave amplitude.

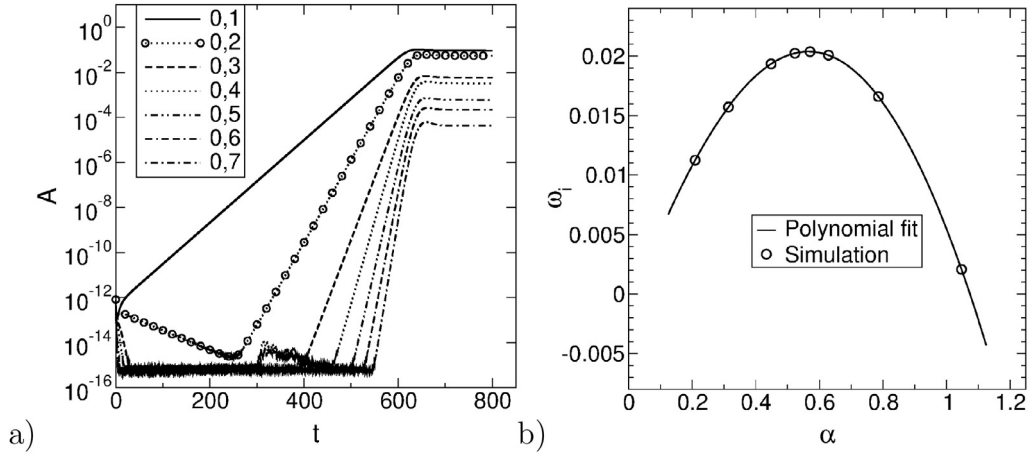

Fig. 17. a) Amplitude vs. time for primary wave & higher harmonics and b) growth rate of 2-D mode versus streamwise wavenumber for case 2.

4. Conclusions

The primary buoyancy-driven instability of Rayleigh-Bénard-Poiseuille flow leads to the development of counter-rotating longitudinal vortices that are aligned in the streamwise direction. Upon saturation of the primary mode, secondary instability can lead to a sinusoidal waviness of the longitudinal rolls as observed in the experiments by Pabiou et al. [12]. The majority of the literature concerned with the secondary instability investigation of plane RBP flows is for channels with finite spanwise extent likely because of their research prevalence in technical applications. This paper demonstrates how temporal stability simulations based on the full and linearized Navier-Stokes equations (DNS and LNS) can be employed for investigating the secondary instability of RBP flows with infinite spanwise extent. The present LNS results serve to cross-validate the DNS results and demonstrate the utility of LNS for secondary instability analyses. The present stability simulations were carried out with two highly accurate research codes by Hasan and Gross [15].

The secondary instability investigations were performed for three cases with buoyancy-driven primary instability. A validation case was computed first. The streamwise wavelength and phase speed of the most strongly amplified secondary unstable wave were in good agreement with the reference data by Clever and Busse [10] and Pabiou et al. [12]. The growth rates of the unstable two-dimensional (2-D) and three-dimensional (3-D) secondary modes obtained from simulations based on the full and linearized Navier-Stokes equations were in excellent agreement which proves that the secondary growth is in fact linear. Similar to resonance triads for fundamental boundary layer breakdown [18], the secondary instability was found to result from a triad interaction of the fundamental steady 3-D mode with a 2-D and two oblique modes. The secondary instability was shown to lead to a sinusoidal waviness of the longitudinal rolls as observed in the experiments by Pabiou et al. [12]. The analysis also demonstrated that the longitudinal rolls resulting from the primary instability need to be fully developed in order for the sinusoidal secondary instability to occur. Moreover, the simulations showed that the secondary instability becomes weaker and the streamwise wavelength of the wavy mode is increased when the Rayleigh number is lowered.

The present results illustrate that carefully set up temporal stability simulations constitute an alternative to linear stability investigations based on a normal mode ansatz. For the present geometrically simple problem, the DNS and LNS codes are computationally less efficient than analyses based on linear or weakly non-linear stability theory, such as biglobal stability analysis. However, one could conceive geometrically more complex and/or non-linear problems where linear or weakly non-linear theory is no longer possible and/or applicable. In such instances, temporal stability simulations can provide useful insight into the primary or secondary instability or non-linear interactions.

Declaration of Competing interests

The authors declare that they have no known competing financial interests or personal relationships that could have appeared to influence the work reported in this paper.

CRediT authorship contribution statement

Md Kamrul Hasan: Conceptualization, Data curation, Formal analysis, Investigation, Methodology, Software, Validation, Visualization, Writing - original draft, Writing - review & editing.

Andreas Gross: Conceptualization, Methodology, Software, Validation, Funding acquisition, Project administration, Resources, Writing - original draft, Writing - review & editing.

Acknowledgments

This material is based upon work supported by the National Science Foundation under grant no. 1510179. The program manager is Dr. Ronald Joslin.

Supplementary material

Supplementary material associated with this article can be found, in the online version, at doi:10.1016/j.ijheatmasstransfer.2020.120098.

References

[1] H.F. Fasel, F. Meng, E. Shams, A. Gross, CFD analysis for solar chimney power plants., Sol. Energy 98 (Part A) (2013) 12–22, doi:10.1016/j.solener.2013.08.029.
[2] K.F. Jensen, E.O. Einset, D.I. Fotiadis, Flow phenomena in chemical vapor deposition of thin films., Annu. Rev. Fluid Mech. 23 (1991) 197–233, doi:10.1146/annurev.fl.23.010191.001213.
[3] G. Evans, R. Greif, Thermally unstable convection with applications to chemical vapor deposition channel reactorst., Int. J. Heat Mass Transf. 36 (11) (1993) 2769–2781, doi:10.1016/0017-9310(93)90096-O.
[4] K.S. Gage, W.H. Reid, The stability of thermally stratified plane Poiseuille flow., J. Fluid Mech. 33 (1) (1968) 21–32, doi:10.1017/S0022112068002326.
[5] S.A. Orszag, Accurate solution of the Orr-Sommerfeld stability equation., J. Fluid Mech. 50 (4) (1968) 689–703, doi:10.1017/S0022112071002842.
[6] K. Fujimura, R.E. Kelly, Stability of unstably stratified shear flow between parallel plates., Fluid Dyn. Res. 2 (4) (1988) 281–292, doi:10.1016/0169-5983(88)90006-8.
[7] J.-M. Luijkx, J.K. Platten, J.C. Legros, On the existence of thermoconvective rolls, transverse to a superimposed mean Poiseuille flow., Int. J. Heat Mass Transf. 24 (7) (1981) 1287–1291, doi:10.1063/1.3006057.
[8] M.Y. Chang, C.H. Yu, T.F. Lin, Changes of longitudinal vortex roll structure in a mixed convective air flow through a horizontal plane channel: an experimental study., Int. J. Heat Mass Transf. 40 (2) (1997) 347–363, doi:10.1016/0017-9310(96)00098-1.
[9] M.Y. Chang, T.F. Lin, Experimental study of aspect ratio effects on longitudinal vortex flow in mixed convection of air in a horizontal rectangular duct., Int. J. Heat Mass Transf. 41 (4–5) (1998) 719–733, doi:10.1016/S0017-9310(97)00165-8.
[10] R.M. Clever, F.H. Busse, Instabilities of longitudinal rolls in the presence of Poiseuille flow., J. Fluid Mech. 229 (1991) 517–529, doi:10.1017/S0022112091003142.
[11] Y. Kato, K. Fujimura, Prediction of three-dimensional breakdown of a longitudinal roll in a square duct., Theoretical and Applied Mechanics 50 (2001) 327–333.
[12] H. Pabiou, S. Mergui, C. Bénard, Wavy secondary instability of longitudinal rolls in Rayleigh-Bénard-Poiseuille flows., J. Fluid Mech. 542 (2005) 175–194, doi:10.1017/S0022112005006154.
[13] S. Xin, X. Nicolas, P.L. Quéré, Stability analyses of longitudinal rolls of Poiseuille-Rayleigh-Bénard flows in air-filled channels of finite transversal extension., Numerical Heat Transfer, Part A: Applications 50 (5) (2006) 467–490, doi:10.1080/10407780600620079.
[14] X. Nicolas, N. Zoueidi, S. Xin, Influence of a white noise at channel inlet on the parallel and wavy convective instabilities of Poiseuille-Rayleigh-Bénard flows., Physics of Fluids 24 (8) (2012) 084101(1–28), doi:10.1063/1.4737652.
[15] M.K. Hasan, A. Gross, Higher-order-accurate numerical method for temporal stability simulations of Rayleigh-Bénard-Poiseuille flows., Int. J. Numer. Methods Fluids (2020), doi:10.1002/fld.4877.
[16] H. Fasel, U. Konzelmann, Non-parallel stability of a flat-plate boundary layer using the complete Navier-Stokes equations., J. Fluid Mech. 221 (1990) 311–347, doi:10.1017/S0022112090003585.
[17] M.Y. Chung, H.J. Sung, A.V. Boiko, Spatial simulation of the instability of channel flow with local suction/blowing., Physics of Fluids 9 (11) (1997) 3258–3266, doi:10.1063/1.869423.
[18] A.D.D. Craik, Non-linear resonant instability in boundary layers., J. Fluid Mech. 50 (1971) 393–413, doi:10.1017/S0022112071002635.
[19] J.C.R. Hunt, A.A. Wray, P. Moin, Eddies, stream and convergence zones in turbulent flows., Proceedings of the Summer Program 1988 (1988) 193–208.
[20] P. Wassermann, M. Kloker, Mechanism and passive control of crossflow-vortex-induced transition in a three-dimensoinal boundary layer., J. Fluid Mech. 456 (2002) 49–84, doi:10.1017/S0022112001007418.
[21] G. Bonfigli, M. Kloker, Secondary instability of crossflow vortices: validation of the stability theory by direct numerical simulation., J. Fluid Mech. 583 (2007) 229–272, doi:10.1017/S0022112007006179.
[22] V. Malatesta, L.F. Souza, J.T.C. Liu, M. Kloker, Heat transfer analysis in a flow over concave wall with primary and secondary instabilities., Procedia IUTAM 14 (2015) 487–495, doi:10.1016/j.piutam.2015.03.077.

[23] L.F. Souza, On the odd and even secondary instabilities of gönrtler vortices., Theor. Comput. Fluid Dyn. 31 (2017) 405–425, doi:10.1007/s00162-017-0431-3.
[24] D.S. Park, P. Huerre, Primary and secondary instabilities of the asymptotic suction boundary layer on a curved plate., J. Fluid Mech. 283 (1995) 249–272, doi:10.1017/S0022112095002308.
[25] D. Rodríguez, V. Theofilis, Massively parallel solution of the biglobal eigenvalue problem using dense linear algebra., AIAA Journal 47 (10) (2009) 2449–2459, doi:10.2514/1.42714.
[26] E.M. Gennaro, D. Rodríguez, M.A.F. Medeiros, V. Theofilis, Sparse techniques in global flow instability with application to compressible leading-edge flow., AIAA Journal 51 (9) (2013) 2295–2303, doi:10.2514/1.J051816.